Spatial charge separation on strongly coupled 2D-hybrid of rGO/La$_2$Ti$_2$O$_7$/NiFe-LDH heterostructures for highly efficient noble metal free photocatalytic hydrogen generation

Ramireddy Boppella[a,b], Chi Hun Choi[a], Jooho Moon[b,*], Dong Ha Kim[a,*]

[a] Department of Chemistry and Nano Science, Ewha Womans University, 52, Ewhayeodae-gil, Seodaemun-gu, Seoul 03760, Republic of Korea
[b] Department of Materials Science and Engineering, Yonsei University, 50 Yonsei-ro Seodaemun-gu, Seoul 03722, Republic of Korea

ARTICLE INFO

ABSTRACT

Developing photocatalysts with effective charge separation and fast surface reaction kinetics is crucial to realizing efficient photocatalytic water splitting. In this study, we report a strongly coupled two-dimensional-ternary-heterostructured photocatalyst by sequentially introducing reduced graphene oxide (rGO) and NiFe-layered double hydroxide (NiFe-LDH) on the surface of lanthanum titanate (LTO) via a facile hydrothermal and electrostatic self-assembly methodology, respectively. The synthesized 2D-rGO/LTO/NiFe-LDH photocatalyst showed remarkable photocatalytic H$_2$ evolution activity under simulated light irradiation, even without expensive Pt cocatalyst. The enhancement of photocatalytic activity could be attributed to the efficient interfacial charge transfer at the rGO/LTO heterojunction interface, and the enhanced hole (h$^+$) trapping ability of NiFe-LDH cocatalyst at the LTO/NiFe-LDH interface, respectively. These attributes could effectively enlarge the life time of photo-generated electron-hole pairs, and increase the electron density for hydrogen production. The optimal rGO/LTO/NiFe-LDH nanocomposite remain sustained even after four successive experimental runs, without apparent change in the H$_2$ evolution rate. The present work elucidates a new strategy to maximize the efficiency via synergetic effect of incorporating rGO and NiFe-LDH as dual cocatalysts, and shows a feasible strategy of using earth-abundant materials as cocatalysts to enhance the overall photocatalytic water splitting reactions.

1. Introduction

The utilization of renewable solar energy to drive hydrogen (H$_2$) evolution by water splitting is an attractive and environmentally friendly solution to mediate the current global energy crisis [1–3]. Recently, much attention has been given to the layered perovskite photocatalysts, owing to the large surface to volume ratio, excellent chemical stability, low cost, and low toxicity [4–6]. In particular, lanthanum titanate (La$_2$Ti$_2$O$_7$, LTO), one of the layered perovskite oxides, has attracted significant interest from the scientific community as a versatile photocatalytic platform to perform water splitting, due to its suitable band gap, appropriate band edge positions, and economical production cost [4,7–9]. However, striking demonstration of water splitting with LTO has been limited, due to its low light-harvesting ability (band gap of (∼3.2–3.6) eV), poor charge transport property, and slow interfacial kinetics for water oxidation, which inherently result in the low solar-to-hydrogen conversion efficiency of LTO [8–11].

Researchers have employed various different strategies to extend the light responsivity and activity of LTO into the visible region by doping with foreign elements [12], constructing heterojunctions [5,7,13], and sensitizing with noble metals [8,9], to improve the overall photocatalytic performance. Despite such endeavour, more strategies and research demonstrations are required to improve the charge separation and sluggish surface reactions, in order to design effective photocatalysts for the overall water splitting [14].

Among various strategies for increasing the photocatalytic performance for water splitting, cocatalysts modification is an effective strategy to simultaneously tackle the charge separation and surface reaction on photocatalyst surface [15–17]. The integration of cocatalyst can promote the water splitting mechanism, as it collect the photo-generated charge carriers, constructs catalytic sites, and reduces activation energy for gas evolution [15–17]. Platinum (Pt) is widely considered to be one of the most efficient reduction cocatalysts/electron sinks; however, scarcity and high cost hamper its practical, industrial

---

scale applications. Thus, the development of novel, active, and earth-abundant cocatalyst that can facilitate water splitting is highly desirable [18]. The required criteria for designing the cocatalyst are efficient electron/hole mobility and rapid redox capability, along with the appropriate interfacial contacting sites with the photocatalyst of choice [19]. It has been widely demonstrated that the addition of 2D graphene can greatly improve the catalytic activity of various photocatalysts, by functioning as efficient electron mediator to promote the photo-generated charge separation and transfer [20–24]. Due to its unique charge carrier mobility, large specific surface area, and chemical stability, graphene has been utilized as cocatalyst for H_2 evolution, electron mediator/transporter to suppress the photogenerated charge recombination over semiconductor [22,25–28]. On the basis of the above analysis, the loading of 2D graphene on the surface of 2D LTO NSs could effectively improve the separation/migration of photogenerated charge carriers, and thereby improve H_2 generation.

The photocatalytic water oxidation is a kinetically sluggish reaction, considered to be the bottleneck of the water-splitting process. The invention of viable water oxidation cocatalysts is particularly crucial for the development of light-driven water splitting over a given phtoocatalyst [29–31]. Recently, 2D-layered double hydroxides (LDHs) materials appeared to be stable and effective oxygen evolution cocatalysts (OEC) for photocatalytic or photoelectrochemical water splitting reactions [32–34]. Among the well-known LDH OECs, nickel–iron-layered double hydroxide (NiFe-LDH) has emerged as a promising OER catalyst, owing to its earth abundance, extraordinary intrinsic catalytic activity, and the advantageous unique 2D structure [35,36]. Despite widespread investigations of NiFe-LDH as electrochemical water oxidation catalyst, only a few studies have shown that NiFe-LDH can serve as the active cocatalyst in water splitting reactions [37–40]. Considering the remarkable benefits, it is expected that NiFe-LDH functions as a hole (h^+) *collector* to selectively separate hole from photo-generated electron-hole pairs, and further integration of rGO not only optimizes the interaction between the photocatalyst and the OER catalyst, but also enhances the overall catalytic efficiency, by reducing the recombination rate [21].

Herein, we develop a strongly coupled 2D-ternary hybrid photocatalyst for efficient photocatalytic water splitting reaction, in which 2D NiFe-LDH and ultra-thin rGO were coupled with LTO photocatalyst. Owing to the two-dimensional configuration and the strong electronic coupling between these three components, the rGO/LTO/NiFe-LDH architecture ensure a large external surface area for fast catalytic reaction, effective interfacial charge separation, and short carrier diffusion length for excellent charge transport. The 2D rGO/LTO/NiFe-LDH heterostructure showed remarkable performance for photocatalytic H_2 generation under simulated solar irradiation, without the need for expensive Pt. The synergistic effect of rGO and NiFe-LDH as dual cocatalysts improve the photocatalytic activity, where NiFe-LDH mainly traps the holes from the valence band of LTO, and improves the water oxidation properties, while the rGO functions as an electron mediator to capture and transport photogenerated electrons from the conduction band (CB) of LTO, leading to the reduction of protons to hydrogen.

2. Experimental section

2.1. Materials

Nickel (II) nitrate hexahydrate ($Ni(NO_3)_2 \cdot 6H_2O$), Iron (III) nitrate hexahydrate ($Fe(NO_3)_3 \cdot 6H_2O$), lanthanum nitrate hexahydrate (La($NO_3)_3 \cdot 6H_2O$), potassium permanganate ($KMnO_4$), sodium nitrate ($NaNO_3$) and Nafion® (Sigma Aldrich, 5 wt.% in mixture of lower aliphatic alcohols and water, contains 45% water) were purchased from Sigma Aldrich. Titanium sulfate ($Ti(SO_4)_2$) was obtained from Tokyo Chemical Industry. NaOH and Na_2CO_3 were purchased from Daejung Chemicals. All the chemicals were used without further purification.

2.2. Synthesis of $La_2Ti_2O_7$ nanosheets

The $La_2Ti_2O_7$ nanosheets (NS) were prepared via hydrothermal synthesis. Briefly, 20 mM of La($NO_3)_3 \cdot 6H_2O$ and 20 mM Ti($SO_4)_2$ were dissolved in 25 mL deionized water, with constant stirring to form a homogeneous solution. Then, 5 mL of 2 M NaOH aqueous solution was added to the above homogeneous solution, under rapid stirring. The mixture was stirred for another 10 min, before transferring into the 50 mL Teflon-lined autoclave. The solution was heated at 200 °C for 24 h, and was naturally cooled to room temperature. The resultant precipitate was collected, and was washed several times with deionized water. The final product was dried overnight at 60 °C.

2.3. Synthesis of NiFe LDH

The synthesis of NiFe-LDH was synthesized by facile co-precipitation method at room temperature with a molar ratio of Ni/Fe = 3:1. Briefly, 1.2 M of Ni($NO_3)_2 \cdot 6H_2O$ and 0.4 M of Fe($NO_3)_3 \cdot 9H_2O$ were dissolved in 200 mL of deionized water. Subsequently, 50 mL of solution containing 0.05 M NaOH/0.05 M Na_2CO_3 was added. The suspension was stirred for 24 h at 80 °C, washed three times with water, and dried at 60 °C. As-prepared NiFe-LDH was re-suspended in water (1 mg/mL), and exfoliated by sonication for 6 h, to obtain a stable exfoliated NiFe-LDH suspension. During the period of catalytic assessment the obtained NiFe-LDH materials were confirmed stable, without any noticeable signs of agglomeration. The homogenous suspension exhibited a positive zeta potential of ~ 32 mV, which was ascribed to the presence of both divalent and trivalent metal cations on the surface of LDH.

2.4. Synthesis of graphene oxide (GO)

Graphene oxide (GO) was synthesized via a modified Hummers method, as described in our previous report [22]. In summary, graphite flakes (1 g) was added to the flask containing 70 mL of H_2SO_4 in the ice bath. $KMnO_4$ (3 g) and $NaNO_3$ (0.5 g) were then added slowly to the overall solution. The mixture was stirred for 4 h, and deionized water (100 mL) was carefully added to the mixture. The resulting mixture was maintained at constant temperature for 30 min. Then, 30 mL of H_2O_2 solution (30%) was gradually added into the solution while stirring, until the suspension turned to brilliant brown, indicating the complete oxidization of graphite. The resulting suspension was washed with a mixture of HCl and deionized water, to remove the remaining metal ions. The final product was repeatedly washed with deionized water, until the pH of the filtrate became neutral. The resulting GO slurry was freeze-dried, and stored in a desiccator. The obtained graphite oxide powder was added to deionized water (1 mg/mL), and exfoliated through sonication for 6 h. The resultant suspension was centrifuged for 30 min at 3000 rpm to remove any precipitates. The supernatant was collected as the final GO solution. The resulting GO solution displayed a Zeta potential of ~ 29 mV.

2.5. Synthesis of rGO/LTO

In a typical preparation of rGO/LTO, 100 mg of LTO was dispersed in 50 mL of deionized water under ultrasonic treatment with the appropriate amount of GO (5 mg/mL) suspension. The resulting suspension was transferred to a Teflon-lined stainless steel autoclave, sealed, and heated at 180 °C for 6 h. The autoclave was cooled to room temperature to obtain rGO/LTO. Subsequently, rGO/LTO sample was washed several times with deionized water, and then dried overnight at 60 °C. Zeta potential measurements confirmed the LTO nanosheets had a Zeta potential of ~ 17 mV.

2.6. Synthesis of LTO/NiFe-LDH and rGO/LTO/NiFe-LDH

For the synthesis of LTO/NiFe-LDH composites, 100 mg of LTO was

dispersed in 100 mL of deionized water in the ultrasonic bath for 30 min. The desired amount of NiFe-LDH suspension was added to LTO, and stirred for another 24 h to obtain LTO/NiFe-LDH. A self-assembly technique was employed to construct the LTO/NiFe-LDH composites through the electrostatic interaction between LTO and NiFe-LDH, as suggested through the Zeta potential analysis. To synthesize rGO/LTO/NiFe-LDH composite, the overall synthesis procedure was identical to synthesizing LTO/NiFe, except LTO was replaced by rGO/LTO. To investigate the role of the ternary composition in the photocatalytic performances, the amounts of rGO and NiFe-LDH were varied to obtain $rGO_{1-x}/LTO/NiFe_{1-x}$ heterostructures with different mass ratios, where x represents the different weight amount of rGO and NiFe-LDH.

2.7. Characterization

The surface morphology was characterized using scanning electron microscopy (SEM; JEOL JSM-7800) and transmission electron microscopy (TEM; JEOL JSM-2100 F operated at 200 kV). The crystalline structures of the materials were investigated by X-ray diffraction (XRD; Rigaku Dmax 2000, diffractometry using Ni filtered Cu Kα radiation (λ = 1.5418 Å)) in the 2θ region between (10 and 70) ˚C, to elucidate the crystallinity and phase structure between the layers. UV–vis absorbance and diffuse reflectance spectra (DRS) were measured by Varion 5000 spectrometry. X-ray photoelectron spectroscopy (XPS) spectra were measured on the Thermo Scientific K-Alpha XPS, using a dual beam source and ultra-low energy electron beam for charge compensation. The FTIR spectra of the samples were recorded on a Bruker Alpha FTIR spectrophotometer at room temperature taking a KBr as a reference sample. The PL spectra were recorded on a Perkin Elmer LS55 Fluorescence spectrophotometer with an excitation energy of 360 nm.

2.8. Evaluation of photocatalytic performance

The hydrogen evolution was carried out in an air-tight quartz reactor under AM 1.5 illumination (100 mW/cm^2). The photocatalyst (20 mg) was suspended in 40 mL of solution containing deionized water, and 10 vol.% triethanolamine (TEOA) in 70 mL quartz reactor; TEOA was used as the hole scavenger for the hydrogen evolution reaction. For the O_2 evolution, the experimental condition was identical to the aforementioned procedure, except 0.01 M $NaIO_3$ was used as the electron scavenger instead of TEOA. The reactor was sealed with a rubber septum, and purged with N_2 gas for 30 min, before initiating the irradiation. The simulated solar irradiation, AM 1.5 (100 mW·cm^{-2}), was illuminated through the quartz glass window for a period of three hours, and the amount of H_2 gas was recorded every 1 h interval, for which 1 mL of gas was extracted by a gas-tight micro syringe, and the amount of H_2 was analysed by gas chromatography (GC; Shimadzu GC-2014, Molecular sieve 5 Å Column) equipped with thermal conductivity detector (TCD) detector.

2.9. Photoelectrochemical measurements

First, 20 mg of photocatalyst powder was mixed with 500 μL of deionized water, 500 μL of ethanol, and 100 μL of Nafion®. The overall mixture was treated with ultrasound sonication, until the homogeneous suspension was formed. The resultant suspension was deposited onto the fluorine-doped tin oxide (FTO) substrate with an active area of 1 cm^2. The resulting photoelectrode was then dried on a hot plate at 100 ˚C for 12 h under the ambient condition. The photoelectrochemical (PEC) measurements were conducted in a three-electrode system using a potentiostat (Autolab ECO Chemie PGSTAT302N), with the photoelectrode as the working electrode, Ag/AgCl (3 M KCl) as the reference, and Pt foil as the counter electrode; 1 M NaOH aqueous solution was employed as the electrolyte (pH = ~13.6). The measured potentials were converted with respect to the reversible hydrogen electrode (RHE)

scale using the Nernst equation. Electrochemical impedance spectra (EIS) were recorded at the open circuit voltage, and at a potential frequency range of (1 MHz to 0.1 Hz), with an AC amplitude of 10 mV. The collected EIS data were fitted to the equivalent circuit model using ZView software (Scribner Associates). Mott–Schottky measurements were performed using an electrochemical analyser (IVIUMSTAT.XR, IVIUM Technologies).

3. Results and discussion

The preparation process for rGO/LTO/NiFe-LDH composite photocatalyst was constructed through three major synthesis methods: the graphene oxide (GO) by the modified Hummers' method, NiFe-LDH nanosheets via co-precipitation, and LTO through a hydrothermal method (see Experimental Section), respectively. A mixture containing specific amounts of GO and LTO nanosheets was then transferred into a Teflon-lined stainless autoclave, which was hydrothermally treated to form 2D rGO/LTO structures. In this step, LTO nanosheets were anchored and encapsulated on rGO nanosheets, while GO was reduced to rGO. Finally, the 2D rGO/LTO was self-assembled through the electrostatic interaction between the NiFe-LDH and rGO/LTO to form the final composite, 2D rGO/LTO/NiFe-LDH photocatalyst.

Detailed morphological studies were conducted using scanning electron microscopy (SEM), and transmission electron microscopy (TEM). Figs. 1a and S1a shows a typical SEM image of LTO nanosheets composed of irregular nanosheets with sizes ranging from (100 to 500) nm. The TEM image further confirms the very thin LTO sheets with average thickness of ~10 nm (Fig. S1a). The high-resolution TEM (HR-TEM) images showed the clear lattice fringes with a d-spacing of 0.277 nm corresponding to the (020) plane of LTO nanosheets (Fig. 1b). The representative TEM images of exfoliated NiFe-LDH revealed a plate-like morphology with a diameter of ~50 nm (Fig. S2). After electrostatic self-assembly of NiFe-LDH with LTO to form LTO/NiFe-LDH composite, NiFe-LDH nanosheets were tightly anchored on the LTO surface, as shown in Fig. 1c and d. A close inspection of HRTEM images confirm the intimate interaction between NiFe-LDH and LTO nanosheets, and showed distinct lattice fringes of 0.277 and 0.25 nm corresponding to (002) and (012) plane of LTO and NiFe-LDH, respectively (Fig. 1e). Elemental mapping measurements further manifest the uniform distribution of Ti, La, Ni, Fe, and O elements throughout the composite structures, as displayed in Fig. S3. Similarly, for the rGO/LTO sample, HR-TEM images revealed that rGO nanosheets are tightly attached to the surface of LTO (Fig. 1f).

A high magnification SEM image display the ternary rGO/LTO/NiFe-LDH composite structures (Fig. S4). Although rGO, NiFe-LDH, and LTO were present in the ternary system, it is difficult to distinguish each component due to the multiple overlapping of rGO and NiFe-LDH. Nevertheless, EDS elemental mapping revealed that the rGO/LTO/NiFe-LDH composite sample composed of C, Ti, La, Ni, Fe, and O elements, and all the elements were evenly distributed in composite structures (Fig. S5). The typical TEM image of ternary rGO/LTO/NiFe-LDH composite also displays two-dimensional structure, and illustrating the existence of close interfacial contact among the three components (Fig. 2a). The different interface interaction between three components were further analysed by HRTEM. Fig. 2b and c obtained from the yellow circles area of Fig. 2a clearly showed a close interfacial contact between rGO/LTO and LTO/NiFe-LDH the components, respectively. EDS elemental mapping further verify the uniform distribution of C, O, Ti, La, Ni, and Fe in the composite structure. These TEM images visibly demonstrated that all the components were indeed well structured and intimately contacted, without any spatial separation. The intimate interface formed between the 2D NiFe-LDH, rGO, and LTO nanosheets in the ternary composite is indeed beneficial for improving charge separation/transportation of photo-generated charge carriers.

Fig. 3a shows the X-ray diffraction patterns of the as-prepared pure LTO nanosheets and composite samples. All diffraction peaks of LTO
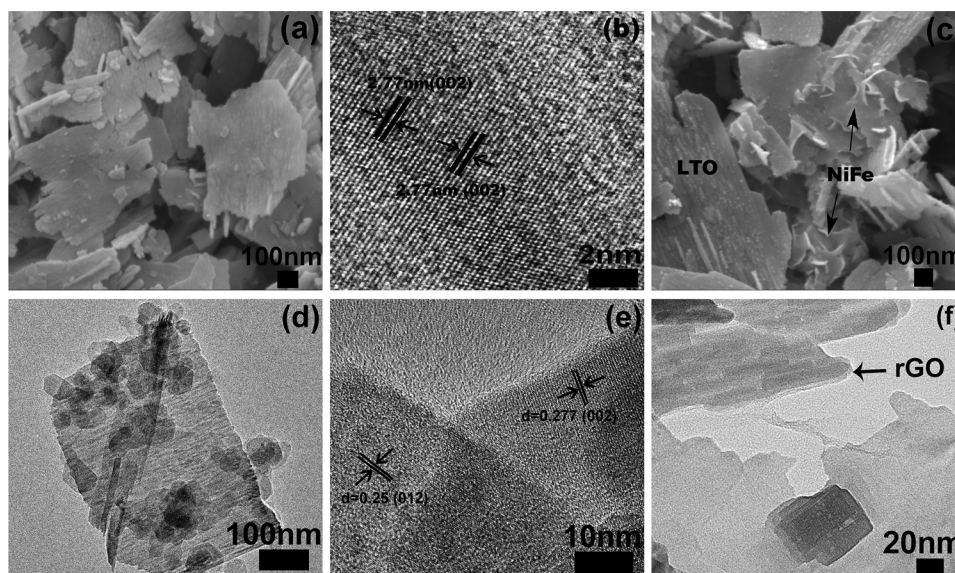
Fig. 1. Morphological images of the as-sysnthesised 2D LTO and its composites; (a) HR-SEM image of LTO, (b)HR-TEM image of LTO, (c) HR-SEM image of LTO/NiFe-LDH, (d) TEM image of LTO/NiFe-LDH, (e) HR-TEM image of LTO/NiFe-LDH and (f) HR-TEM image of rGO/LTO.

and LTO composites exhibits a series of Bragg's diffraction peaks at (32.49, 40.27, 46.85, 58.27, and 68.29)° for the (002), (022), (610), (232) and (235) planes are indexed to the monoclinic phase of $La_2Ti_2O_7$ with the $P2_1$ space group (JCPDS No. 81-1066) [12]. The XRD data of the NiFe-LDH showed weak diffraction peaks at (25.5, 34.9, 60.2, and 71.4)° for the (003), (006), (012), and (110) planes, respectively, which are in good agreement with the previously reported NiFe-LDH [41]. The observed crystal planes are well in agreement with HRTEM results. However, no obvious diffraction peaks for rGO and NiFe-LDH were detected in the composite samples (LTO/NiFe-LDH and rGO/LTO/NiFe-LDH), because of the weak diffraction intensity and small loading amount [20,42,43]. This phenomenon could also be explained by the fact that ultrathin NiFe-LDH and rGO were uniformly distributed on the LTO nanosheets, as shown in the TEM images above (Fig. 2). To demonstrate the intercalation and bonding nature of NiFe-LDH and rGO with the LTO nanosheets, Raman spectra were collected from the (50 to 2000) cm^{-1} region, to detect the specific vibrational modes of the prepared samples. Fig. 3b shows that several peaks below 1000 cm^{-1} were detected, which correspond to the vibrational modes of LTO. After the incorporation of rGO, two distinctive carbon bands around (1340 and 1602) cm^{-1} (D band and G band, respectively) are observed in rGO/LTO and rGO/LTO/NiFe, further confirming the presence of rGO [44]. Also, a positive shift of the D band position from (1321 to 1340) cm^{-1} is found after the incorporation of rGO with LTO/NiFe, signifying the efficient charge transfer in the ternary system. For NiFe-LDH, the

material exhibited bands at 523 cm^{-1}, which were assigned to the stretching vibration of Ni−OH in LDH materials [45]. However, no characteristic vibrational modes of NiFe-LDH were detected, possibly due to the overlap between the peak at 523 cm^{-1} and the characteristic vibrational modes of LTO at ~530 cm^{-1}.

The interaction between rGO, NiFe and LTO nanosheets in composites structure were further verified by Fourier transform Infra-Red (FT-IR) spectroscopy as depicted in Fig. S6. All the samples exhibits broad adsorption peak at 3435 cm^{-1} is attributed to O−H stretching modes and another peak located at 1637 cm^{-1} is related to vibration of water molecules adsorbed on the LTO and its composites [46]. The strong peak at 1637 cm^{-1} corresponds to the C═C stretching vibration of rGO in rGO/LTO is partially overlaps with the H−OH bending mode of water [24]. No other characteristic C═O peaks were observed for rGO/LTO, an indication the fully reduction of GO to rGO during a hydrothermal reduction. The bands present at 1425 cm^{-1} and 1359 cm^{-1} for LTO/NiFe-LDH are related to the symmetric and antisymmetric stretching vibrations of residual the carbonate ion groups (CO^{3-}) [46]. The very broad band centered at 1578 cm^{-1} was difficult to assign but may be associated with the vibration mode of M−OH (Ni−OH or Fe−OH) deformation [47]. In addition, the absorption bands traced at low wavenumber region (500–1000 cm^{-1}) can be ascribed to the lattice vibration modes of Me-O and Me-O-Me (M represents Ni, Fe or Ti and La) [24]. All the characteristic peaks of rGO and NiFe-LDH were clearly observed in the resulting rGO/LTO/NiFe-LDH composites, indicating
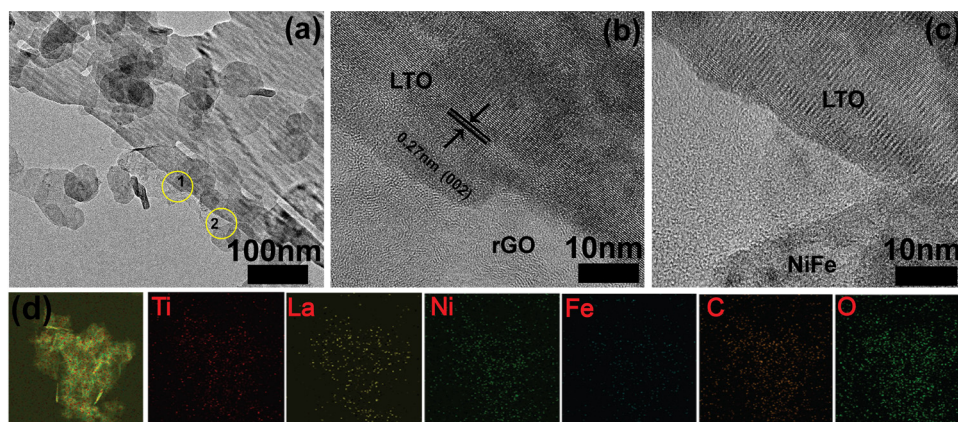
Fig. 2. (a) TEM images of rGO/LTO/NiFe-LDH composite structures, (b) HR-TEM image obtained from the yellow circle area (1) of figure (a) showing the strong interface between rGO and LTO, (c) HR-TEM image obtained from the yellow circle area (2) of figure (a) showing the strong interface between LTO and NiFe-LDH, and (d) HAADF-STEM image and EDX elemental mapping of corresponding elements (For interpretation of the references to colour in this figure legend, the reader is referred to the web version of this article).
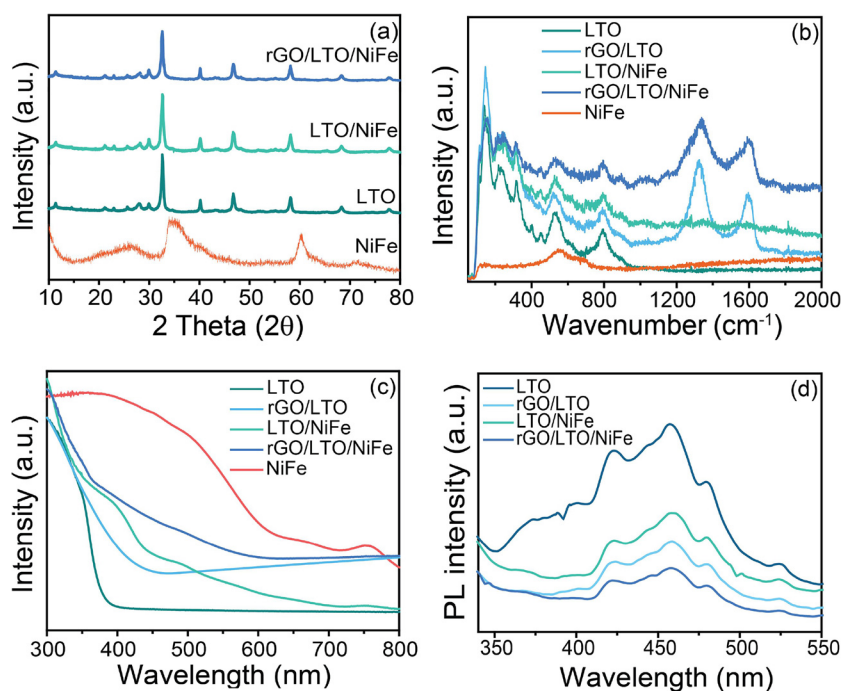
Fig. 3. Structural and optical properties of LTO and its composite photocatalysts. (a) XRD, (b) Raman spectra, (c) UV–vis diffuse reflectance spectra, and (d) photoluminescence spectra of the LTO composite photocatalysts.

the strong interaction between all components. Such strong interactions may significantly improve the charge transfer and expected synergistic effect to enhance the photocatalytic activity.

The optical properties of LTO and its composite structures were investigated by UV–vis diffuse reflectance spectroscopy (DRS), as the photocatalytic activity is highly dependent on the optical absorption characteristics. Fig. 3c shows that the LTO nanosheets exhibit strong absorption in the UV light region with a sharp absorption edge around 390 nm, equivalent to a band gap energy of 3.17 eV is in good agreement with previous reports [9,13]. NiFe-LDH nanosheets showed a strong absorption capability across the visible light region. By making the composite photocatalysts with NiFe-LDH, the resultant final materials exhibited significant enhancement in the visible light absorption. Similar enhancements of visible-light absorption were also evinced for the rGO/LTO composite, owing to the visible light absorption of rGO is in good agreement with the previously reported graphene-based composites [22]. The photoluminescence (PL) measurements were conducted to explore the recombination of photoinduced electron–hole pairs, and transfer of photo-generated charge carriers in the samples. As showed in Fig. 3d, LTO nanosheets exhibited three emission peaks at centered at 421, 458, and 481 nm, which are attributed to the band to band transition and the different charge transfer transition, respectively [48,49]. After the incorporation of NiFe-LDH, rGO, and co-deposition of NiFe-LDH and rGO, the PL intensity of these three peaks apparently decreases, indicating that the efficient charge separation for the heterostructure 2D composite photocatalysts. The excellent electron conductivity of rGO act as an electron transporter, thereby reducing the charge recombination, and the simultaneous integration of NiFe-LDH showed that the recombination of photogenerated electron-hole pairs is effectively suppressed.

The surface elemental composition and the effective interfacial interaction between rGO and NiFe-LDH with LTO were further investigated by X-ray photoelectron spectroscopy (XPS). Fig. S7 shows the Ti, La, Ni, Fe, C, and O peaks in the survey spectrum of rGO/LTO/NiFe-LDH photocatalyst. Fig. 4a shows the high resolution Ti 2p XPS spectra of LTO and its composites, which are deconvoluted to two Ti $2p_{3/2}$ and Ti $2p_{1/2}$ peaks at (458.09 and 463.8) eV, respectively [20,22,23].

Fig. 4b shows that the La 3d XPS spectra of four samples exhibit two doublets, which are ascribed to the spin-orbital splitting of the $3d_{5/2}$ and $3d_{3/2}$ states of La^{3+}. Upon the incorporation of rGO, both Ti 2p and La 3d peaks were shifted to higher binding energy regions, suggesting effective charge transfer from rGO to LTO [44]. This can be ascribed to the formation of strong electronic interaction inducing an electron transfer from LTO to rGO [44]. In contrast, the binding energies of Ti 2p and La 3d in the LTO/NiFe-LDH were down-shifted, when compared with the pristine LTO. The consistent shift of Ti 2p binding energies towards a lower binding energy region is relative to the higher binding energy shift of Fe 2p and Ni 2p (Fig. 4c and d) suggest an electron transfer from NiFe-LDH to LTO. Consequently, the binding energies of Ti 2p in rGO/LTO/NiFe are rather close to those of the pristine LTO, due to the combined effect of rGO and the NiFe-LDH.

To elucidate the elemental composition even further, the O 1 s XPS spectra (Fig. S8) were utilized to demonstrate the interaction between the rGO and NiFe-LDH with LTO. The LTO photocatalyst and its composites have two typical O 1s peaks located at (529.3 and 530.7) eV, ascribed to the Ti−O bond in the TiO_6 octahedron and surface-adsorbed OH groups, respectively [50]. In addition, an additional peak at around ∼532.7 eV was detected for the samples that contained rGO species and NiFe-LDH [42,43]. It should be emphasized that the intensity of the (530.7 and ∼532.7) eV peaks increases when rGO and NiFe-LDH are incorporated into the LTO, due to the abundant surface adsorbed hydroxyl groups presented in both rGO and NiFe-LDH [39]. The shoulder peak at 532.7 eV evidenced HO−C of carboxyl species in the presence of rGO and OH-Ni species in the NiFe-LDH [39,51]. Furthermore, the representative core-level spectra of Ni 2p spectrum exhibits two major peaks at binding energies of ∼853.3 and ∼875.5 eV, and other two satellite peaks at ∼862 and 881 eV can be assigned to Ni $2p_{3/2}$ and Ni $2p_{1/2}$, respectively (Fig. 4c) [41]. The high-resolution Fe 2p XPS spectrum can be ascribed to two dominant peaks at binding energies of about ∼711.4 and ∼724.9 eV corresponding to the Fe $2p_{3/2}$ and Fe $2p_{1/2}$, respectively (Fig. 4d) [41]. These results showed that NiFe-LDH shows the typical Ni^{2+} and Fe^{3+} oxidation states in both composite (LTO/NiFe-LDH and rGO/LTO/NiFe-LDH) samples [41,51]. As shown in Fig. 3c and d, the XPS spectrum of Ni 2p and Fe 2 P for LTO/NiFe-
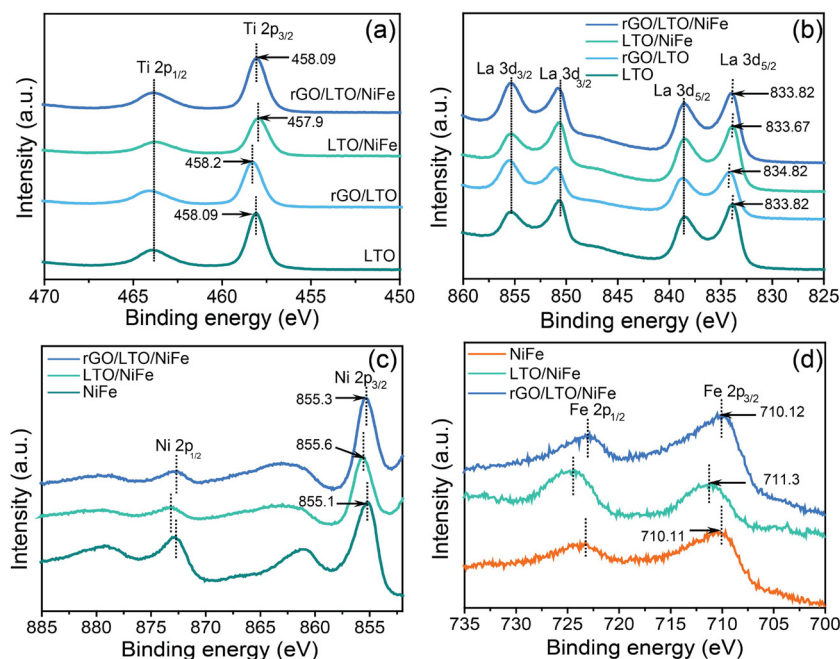
Fig. 4. XPS spectra of (a) Ti 2p, (b) La 3d, (c) Ni 3p, and (d) Fe 2p of LTO, rGO/LTO, LTO/NiFe-LDH, and rGO/LTO/NiFe-LDH.

LDH and rGO/LTO/NiFe-LDH shows a positive shift compared to the NiFe-LDH, confirming the electron transfer from NiFe-LDH to LTO in these two samples. These XPS results clearly demonstrate that the charge transfer process in the composite sample would promote efficient electron-hole separation, and as a result, higher photocatalytic performance.

In order to study the effect of rGO and NiFe-LDH on the surface area and porosity of composite samples, the Brunauer–Emmett–Teller (BET) gas adsorption method was used (Fig. S9). The relative BET specific surface area and total pore volume of samples are listed in Table S1. According to the IUPAC classification, all the samples exhibited the characteristics of type-IV isotherms [52,53]. As shown in Table S2, BET surface area was increases upon the loading of rGO and NiFe-LDH onto the LTO. Furthermore, the pore volume distribution curves illustrate the development of a mesoporous structure in the composite material after the modification, which may be ascribed to the existence of slit-like pores due to the formation of strong interfacial contact. With a large surface area of composites materials offering sufficient interfacial area for more active sites on its surface, which greatly promote the surface redox catalytic reactions and improve the photocatalytic redox reactions.

The photocatalytic H_2 evolution was performed over the synthesized samples in the presence of 10% triethanolamine (TEOA) as a hole (h^+) scavenger under the simulated sunlight. As shown in Fig. 5a and b, a trace amount of H_2 (57.06 µmol g^{-1} h^{-1}) was detected when a pure LTO was used as a photocatalyst under simulated solar irradiation, suggesting the fast recombination of photo-generated charges in pure LTO. In contrast, after the introduction of either rGO or NiFe-LDH into LTO, the obtained rGO/LTO and LTO/NiFe-LDH photocatalysts exhibited remarkably enhanced photocatalytic activity for H_2 evolution. The enhanced H_2 evolution of rGO/LTO can be ascribed to the fact that rGO sheets act as electron mediators that accept the electrons from LTO, and prolong the lifetime of photogenerated electron-hole pairs [22]. The rGO/LTO composite photocatalyst with the optimized rGO loading condition turned out to be 2 wt.% with the high H_2 evolution rate of 291.51 µmol g^{-1} h^{-1} (Fig. S9a). It should be noted that further increase in rGO loading decreased the H_2 evolution performances, suggesting that excessive introduction could have adverse effect, such as decrease in the light absorption efficiency of LTO, by the shielding effect of rGO. For LTO/NiFe-LDH, the photocatalyst exhibited the efficient five-fold enhancement in hydrogen production rate of 355.8 µmol g^{-1} h^{-1} compared to the pristine LTO photocatalysts, with the optimal loading amount of 3 wt.% of NiFe-LDH (Fig. S9b). The suggested hypothesis for such high photocatalytic activity could be
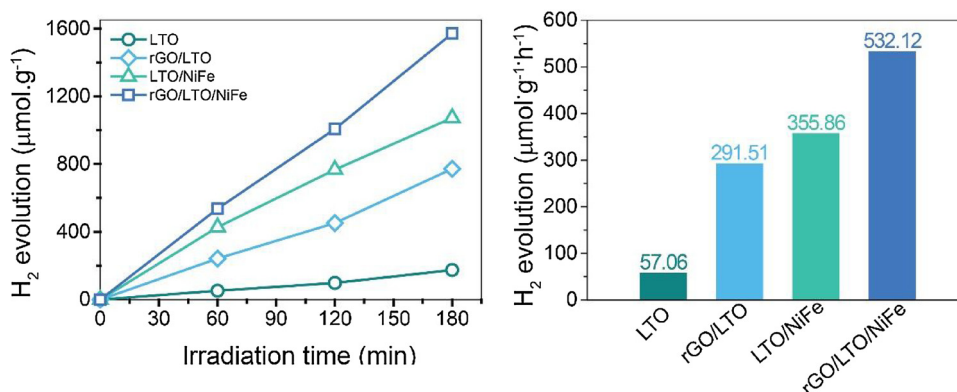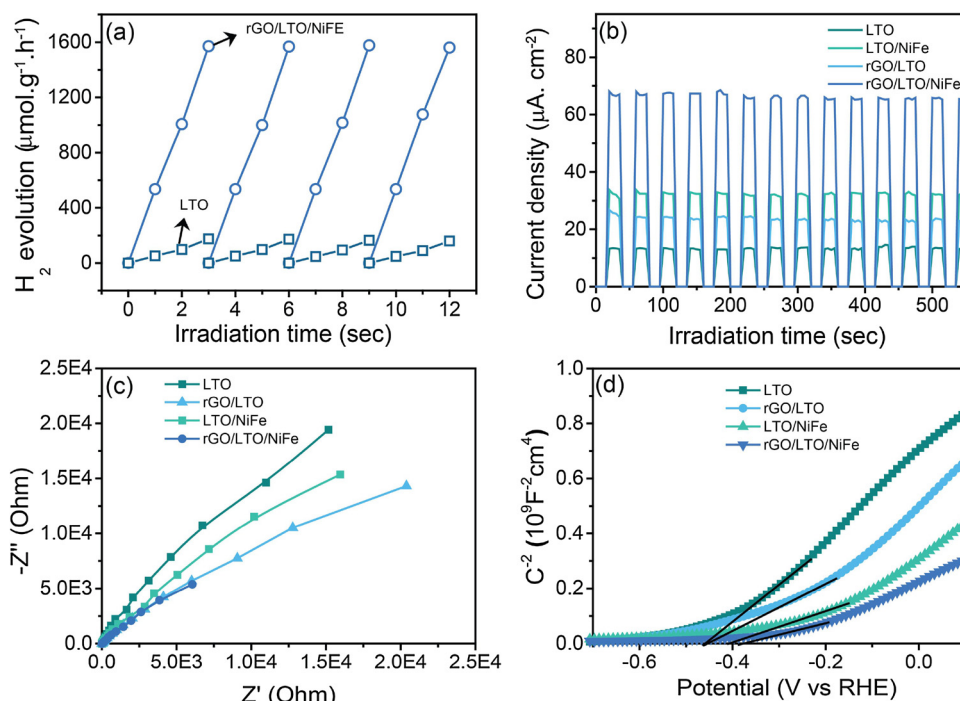

Fig. 5. (a) H_2 production as a function of time over LTO and its composites structures in a aqueous solution containing TEOA solution under simulated light illumination, and (b) comparison of the H_2 evolution rate over LTO, rGO/LTO/ LTO/NiFe-LDH, and rGO/LTO/NiFe-LDH under the same experimental condition.

Fig. 6. (a) The recyclability studies of rGO/LTO/NiFe-LDH for H_2 generation over four consecutive cycles. (b) Transient photocurrent density versus time of LTO, rGO/LTO, LTO/NiFe-LDH, and rGO/LTO/NiFe-LDH under the simulated solar irradiation. (c) EIS Nyquist plots at the open circuit potential under the simulated solar irradiation. (d) Mott–Schottky plots collected at a frequency of 5 kHz in the dark for all the samples.

ascribed to the active hole (h^+) scavenging functionality of the NiFe-LDH cocatalyst on the surface of the LTO to promote the interfacial redox reaction. To evaluate the effect of NiFe-LDH on the photocatalytic performance even further, photocatalytic water oxidation experiment was performed using $NaIO_3$ as the electron acceptor. Fig. S10 shows that the oxygen evolution reaction (OER) was increased with increasing NiFe-LDH concentration, and the best OER rate was achieved with the photocatalyst with 3 wt.% NiFe-LDH. This illustrates that the deposition of NiFe-LDH can trap holes for surface catalytic reactions, to improve the charge separation efficiency. Similar to the rGO/LTO samples, the excessive deposition of NiFe-LDH onto the surface of LTO decreased the OER performance, suggesting that the optimized loading is essential to boost the overall photocatalytic performance. In contrast, individually evaluated NiFe-LDH showed only minor oxygen production activity even after 3 h (Fig. S10).

To further confirm the co-catalytic effect of rGO and NiFe, overall photocatalytic water splitting was assessed under simulated light in the absence of neither TEOA nor $NaIO_3$. No H_2 or O_2 evolution could however be observed for both LTO and rGO/LTO (results are not depicted), suggesting that both catalytic systems were unable to split the water effectively toward photocatalytic H_2 and O_2 evolution in the absence of TEOA and $NaIO_3$ scavengers, respectively. Interestingly, LTO/NiFe-LDH showed a trace amount of O_2 evolution (Fig. S11). The obtained results may reflect a superior efficiency of NiFe as a hole scavenger, facilitating charge separation. Abundant holes trapped by NiFe-LDH may further facilitate O_2 evolution over the LTO/NiFe-LDH catalytic system. Analogous results previously reported may suggest the occurrence of charge recombination following a continuous accumulation of holes in the NiFe co-catalyst with subsequent recombination with the generated electrons [54]. The observation further agrees with the sluggish nature of the water oxidation reaction well-documented in the literature. As a result, both oxygen and hydrogen evolution are thus expected to be decreased after prolonged light illumination. When both rGO(2 wt%.) and NiFe-LDH(3 wt%.) were simultaneously introduced onto the LTO surface, simultaneous H_2 and O_2 evolution were clearly observed. These results underline the potential of rGO/LTO/NiFe-LDH photocatalyst and its promising high electron-hole separation. Nonetheless, considerably low stoichiometric H2/O2 ratio was observed (Fig. S11) and, as the reaction proceed, the rate of H_2 and O_2 evolution

were decreased as a function of time.

In contrast, the H_2 evolution rate became more pronounced when the addition of TEOA hole scavenger as showed in Fig. 5. The superior H_2 evolution activity rate of 532.2 $\mu mol.g^{-1}. h^{-1}$ was attained, which is approximately (9, 1.8, and 1.3) times higher than those of the pristine LTO, rGO/LTO, and LTO/NiFe-LDH, respectively. Such high photocatalytic performance could be ascribed to the fact that the deposition of rGO and NiFe-LDH cocatalysts can efficiently separate photo-generated electrons and holes respectively, and accelerate the surface catalytic reactions. This hypothesis is supported and in accordance with the PL analysis (Fig. 3d), as the PL intensity was significantly decreased when both rGO and NiFe-LDH were introduced to the LTO.

To understand the effect of TEOA hole scavenger on photoactivity, H_2 evolution was performed with different amount of TEOA with and without NiFe-LDH incorporated sample. As showed in Fig. S12, the H_2 evolution of rGO/LTO/NiFe-LDH rapidly increases with increasing TEOA amount, reaches maximum with 5% of TEOA. Notably, the H_2 evolution was found almost independent beyond 5% of TEOA concentration, suggesting that TEOA could not further improve the photocatalytic activity after an optimal concentration. Control experiment without NiFe-LDH (rGO/LTO) showed a gradual increasing in H_2 evolution even 20% of TEOA, indicating a synergistic effect exists between TEOA and NiFe-LDH. These results suggest that NiFe-LDH accelerate the subsequent hole transfer from LTO to TEOA in the solution, underline the role of NiFe-LDH as effective hole scavenger.

Diffuse reflectance UV–Vis absorption studies showed that the incorporation of NiFe and rGO significantly increase the absorption edge of LTO into visible region (Fig. 3c). To assess the possibility of enhanced catalytic efficiency under visible light illumination, the photocatalytic performances of rGO/LTO, LTO/NiFe and rGO/LTO/NiFe were performed under the > 420 range. However, H_2 evolution could not be detected in the corresponding visible region even after 5 h (results not included). Instead, the improved photoactivity of rGO/LTO, LTO/NiFe-LDH and rGO/LTO/NiFe-LDH composites were thus believed to be the result of improved charge separation rather than enhancing carrier generation from the visible light range via enhanced photo absorption [22,39]. The stability of given photocatalyst is a critical issues for the long-term usage for practical applications. The photostability of the synthesized LTO and rGO/LTO/NiFe-LDH nanocomposites were
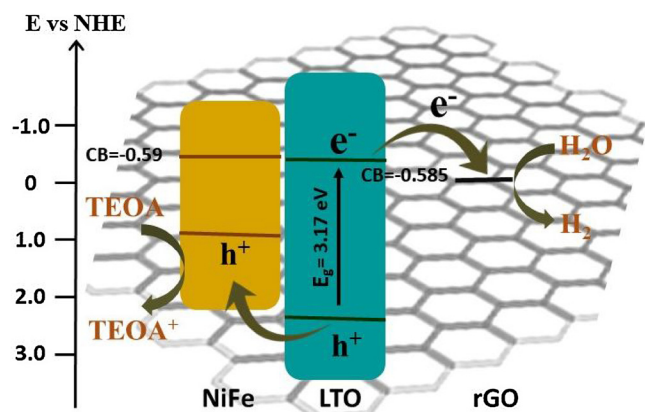
Fig. 7. Proposed mechanism of the charge separation and transfer kinetics in rGO/LTO/NiFe-LDH composite photocatalysts for hydrogen evolution under simulated solar light irradiation.

evaluated for four cycles of H_2 evolution experiments under the same experimental conditions. As showed in Fig. 6a, both the LTO and rGO/ LTO/NiFe-LDH photocatalysts revealed analogues photocatalytic H_2 evolution, even after four consecutive experimental runs (~12 h), retaining over 96% of its initial activity. This result suggests that the synthesized catalyst does indeed possess high photostability, a critical feature for designing an efficient photocatalyst. The slight reduction in activity is originated from the unavoidable loss of the catalyst during the recycling runs.

To elucidate the possible photocatalytic mechanisms, a series of photoelectrochemical approaches were conducted (Fig. 6b–d). First, the prepared photocatalyst materials were deposited on the FTO substrate. Chronoamperometry was used to compare the generated photocurrent transient response of LTO, LTO/NiFe-LDH, rGO/LTO, and rGO/LTO/ NiFe-LDH under simulated solar irradiation at the potential bias of 1.23 V vs. RHE in 1 M NaOH aqueous solution. Fig. 6b shows that all the photoelectrodes display a prompt and reproducible photocurrent response with respect to the on-off cycles, implying efficient light harvesting and charge separation. The pristine LTO photoelectrode exhibits a current density of 13.4 μA·cm^{-2}. After the individual introduction of rGO and NiFe-LDH to LTO, the current densities of the fabricated hybrid photoelectrodes rGO/LTO and LTO/NiFe-LDH increased to 26.5 and 32.33 μA·cm^{-2}, respectively. It is worth noting that the photo-current response of LTO is greatly enhanced with the addition of NiFe-LDH, suggesting that the functional catalytic roles of NiFe-LDH not only to facilitate fast charge carrier transfer, but also to serve as active site for redox reactions [21]. The simultaneous introduction of both rGO and NiFe-LDH to LTO (rGO/LTO/NiFe-LDH) inherently resulted in the highest photocurrent of 66.4 μA·cm^{-2}. The aforementioned results are in excellent accordance with the photocatalytic performance (Fig. 5a and b) and further corroborate the synergistic enhancement in photo-catalytic activity by the simultaneous introduction of rGO and NiFe-LDH. Moreover, the transient photocurrent response of the resulting photoelectrodes shows a prompt and reproducible photocurrent for all evaluated samples, inferring the fast surface reaction kinetics, superior electron–hole separation, and excellent photochemical stability.

The electrochemical impedance spectra (EIS) were recorded with the open circuit potential under simulated light, to evaluate the charge carrier migration of the fabricated photoelectrodes. All the samples exhibit a single semicircle in the high frequency region, as shown in Fig. 6(c). The decrease in radius of the semi-circular EIS Nyquist plots reflecting the charge transfer resistance is significantly suppressed at the electrode interface in the order of LTO, rGO/LTO, LTO/NiFe-LDH, and rGO/LTO/NiFe-LDH, respectively [52,53]. The smallest arch of the rGO/LTO/NiFe-LDH further indicated that the introduction of both rGO nanosheets and NiFe-LDH effectively decreases the overall charge-

transfer resistance at the electrode/electrolyte interface, resulting in an effective separation of photo-generated electron-hole pairs for higher photocatalytic performance.

The Mott–Schottky plots were collected to study the semiconducting properties of the samples. All the synthesized samples exhibited a positive slope for the Mott–Schottky plots, a typical characteristic for n-type semiconductors (Fig. 6d). The flat band potentials were deduced from Mott-schottky analysis, and are closely related to the interfacial charge transfer at the electrode/electrolyte interface, which shows that the larger the flat band potential, the higher the charge transfer [55]. The flat-band potential of LTO/NiFe-LDH showed a cathodic shift compared to both LTO and rGO/LTO samples. This cathodic shift of the flat-band potential suggested that the introduction of NiFe-LDH onto the surface of LTO created the band bending at the electrolyte interface; such a phenomenon is favorable for transferring the photo-generated holes to the surface [56,57]. Notably, the flat-band potential is even further shifted to the positive side for the rGO/LTO/NiFe-LDH photocatalyst, indicating a larger degree of separation of photo-generated electrons and holes [55]. In addition, the rGO/LTO/NiFe-LDH showed relatively smaller slope than those of the other counterparts, which suggests that the former sample has the faster charge transfer kinetics and highest donor density [58,59].

Based on the aforementioned discussion, the suggestive photo-catalytic mechanism was constructed and summarized for the prepared catalysts (Fig. 7). The enhanced H_2 evolution in rGO/LTO/NiFe-LDH is mainly due to the synergistic effect between rGO and NiFe-LDH that simultaneously function as the charge separators for photo-generated electron and hole pairs. To investigate the mechanism involved in the enhanced photocatalytic H_2 reduction on the rGO/LTO/NiFe-LDH heterostructures, the absolute band position of individual component in heterojunction systems, and the direction of photogenerated charge carriers need to be clarified. The valence band edge potential (E_{vb}) and the conduction band edge potential (E_{cb}) of both LTO and NiFe-LDH were calculated by Mulliken electronegativity theory, by using the following empirical equations [5,60];

$$E_{vb} = \chi - E_e + 0.5E_g \qquad (1)$$

$$E_{cb} = E_{vb} + E_g \qquad (2)$$

where, E_{vb} is the valence band edge potential, χ is the absolute electronegativity of the semiconductor, which is determined as the geometric mean of the electronegativity of the constituent atoms, E_e is the energy of the free electrons on the hydrogen scale (4.5 eV), and E_g is the band gap energy of the semiconductor, which can be estimated from the onset of the absorption edge (λ), using the formula $E_g = 1,240/\lambda$ [61,62].

The calculated values of the band gap and absolute electronegativity are (3.17 and 5.5) eV for LTO, and (1.76 and 4.28) eV for NiFe-LDH, respectively. Subsequently, the conduction band (CB) minimum and valence band (VB) maximum were determined to be (-0.585 and 2.58) eV for LTO, and (-0.59 and 1.17) eV for NiFe-LDH, relative to the normal hydrogen electrode (NHE), respectively. It was found that the determined flat band potential of pure LTO (-0.46 V vs RHE) from the Mott–Schottky analysis (assuming the gap between V_{fb} and bottom edge of the conduction band (CB) to be small (~0.2 eV)) was close to the value obtained from the theoretical calculation, and in agreement with the previous results [5,7]. Finally, the determined Fermi level of rGO is 0 V vs NHE, which is lower than the CB minimum of the LTO [26]. Fig. 7 illustrate the schematic energy band diagram represents the charge separation and transfer of charge carriers in the resulting heterojunction for rGO/LTO/NiFe-LDH composites. Upon light irradiation, an electron is excited from the VB of LTO to CB and left the holes in VB. The electrons in the CB of LTO are readily transferred to rGO, as the reduction potential of rGO lies below the CB of LTO, and then effectively reduces proton to produce H2 molecules [50,63,64]. Superior electron mobility and good intimate rGO contact of LTO nanosheets and

could remarkably inhibit the bulk recombination, and enhance the charge transfer/separation efficiency [19,27]. Meanwhile, the resultant holes in the VB of LTO are extracted by NiFe-LDH, as the VB of NiFe-LDH is more positive than that of LTO, leading to the oxidation of Fe^{2+} to Fe^{3+} [39,46,65]. It was reported that the redox potentials of Ni^{3+}/Ni^{2+} and Fe^{3+}/Fe^{2+} were more positive than that of $TEOA^+/TEOA$, and the accumulated holes in NiFe-LDH could be readily captured by TEOA [66,67]. Therefore, NiFe-LDH cocatalyst could function as a hole collector to efficiently remove holes from the VB of LTO, decreasing the overall recombination rate of the photo-generated carriers. Consequently, the co-catalytic effect of rGO and NiFe-LDH simultaneously improved the charge separation, water oxidation efficiency, and photocatalytic performance.

4. Conclusions

In summary, we developed a novel 2D heterostructured photocatalyst by integrating rGO and NiFe-LDH onto LTO nanosheets for efficient H_2 generation. The optimum rGO/LTO/NiFe heterostructure showed the highest H_2 production rate of $532\,\mu mol\,g^{-1}\,h^{-1}$, which is 9 times higher than that of pure LTO. The superior performance of the synthesized 2D composite photocatalyst is ascribed mainly to the synergistic effect of both rGO and NiFe-LDH for suppressing the recombination of photo-generated carriers to drive the desired water splitting reaction. The constructed heterojunctions were highly stable under the simulated solar irradiation, even after four successive experimental runs, with minimal activity lost. This work shows that the careful construction of earth-abundant photocatalyst can be an effective method for inducing the water splitting reaction, stepping closer to the combustion-free energy economy for the future generation.

Notes

The authors declare they have no competing financial interest.

Acknowledgments

Appendix A. Supplementary data

Supplementary material related to this article can be found, in the online version, at doi:https://doi.org/10.1016/j.apcatb.2018.07.063.

References

[1] A. Fujishima, K. Honda, Nature 238 (1972) 37–38.
[2] K. Sivula, R. van de Krol, Nat. Rev. Mater. 1 (2016) 15010.
[3] J. Luo, J.-H. Im, M.T. Mayer, M. Schreier, M.K. Nazeeruddin, N.-G. Park, S.D. Tilley, H.J. Fan, M. Grätzel, Science 345 (2014) 1593–1596.
[4] G. Zhang, G. Liu, L. Wang, J.T.S. Irvine, Chem. Soc. Rev. 45 (2016) 5951–5984.
[5] A. Nashim, K. Parida, J. Mater. Chem. A 2 (2014) 18405–18412.
[6] Y. Miseki, H. Kato, A. Kudo, Energy Environ. Sci. 2 (2009) 306–314.
[7] X. Cai, J. Zhang, M. Fujitsuka, T. Majima, Appl. Catal. B: Environ. 202 (2017) 191–198.
[8] F. Meng, S.K. Cushing, J. Li, S. Hao, N. Wu, ACS Catal. 5 (2015) 1949–1955.
[9] M. Zhu, X. Cai, M. Fujitsuka, J. Zhang, T. Majima, Angew. Chem. Int. Ed. 56 (2017) 2064–2068.
[10] J. Zhang, W. Dang, Z. Ao, S.K. Cushing, N. Wu, Phys. Chem. Chem. Phys. 17 (2015) 8994–9000.
[11] X. Cai, L. Mao, J. Zhang, M. Zhu, M. Fujitsuka, T. Majima, J. Mater. Chem. A 5 (2017) 10442–10449.
[12] F. Meng, Z. Hong, J. Arndt, M. Li, M. Zhi, F. Yang, N. Wu, Nano Res. 5 (2012) 213–221.
[13] Y. Ao, K. Wang, P. Wang, C. Wang, J. Hou, Appl. Catal. B: Environ. 194 (2016) 157–168.
[14] J. Kim, D.W. Hwang, H.-G. Kim, S.W. Bae, S.M. Ji, J.S. Lee, Chem. Commun. 21 (2002) 2488–2489.
[15] J. Yang, D. Wang, H. Han, C. Li, Acc. Chem. Res. 46 (2013) 1900–1909.
[16] X. Li, J. Yu, J. Low, Y. Fang, J. Xiao, X. Chen, J. Mater. Chem. A 3 (2015) 2485–2534.
[17] S. Kumar, K. Ojha, A.K. Ganguli, Adv. Mater. Interf. 4 (2017) 1600981.
[18] Q. Xiang, J. Yu, M. Jaroniec, J. Am. Chem. Soc. 134 (2012) 6575–6578.
[19] H. Yu, J. Tian, F. Chen, P. Wang, X. Wang, Sci. Rep. 5 (2015) 13083.
[20] R. Boppella, J.-E. Lee, F.M. Mota, J.Y. Kim, Z. Feng, D.H. Kim, J. Mater. Chem. A 5 (2017) 7072–7080.
[21] Y. Hou, Z. Wen, S. Cui, X. Feng, J. Chen, Nano Lett. 16 (2016) 2268–2277.
[22] R. Boppella, S.T. Kochuveedu, H. Kim, M.J. Jeong, F. Marques Mota, J.H. Park, D.H. Kim, ACS Appl. Mater. Interfaces 9 (2017) 7075–7083.
[23] C.H. Sung, R. Boppella, J.-W. Yoo, D.-H. Lim, B.-M. Moon, D.H. Kim, J.Y. Kim, Adv. Mater. Interf. 4 (2017) 1700564.
[24] Y. Zhang, W. Cui, W. An, L. Liu, Y. Liang, Y. Zhu, Appl. Catal. B: Environ. 221 (2018) 36–46.
[25] Q. Li, B. Guo, J. Yu, J. Ran, B. Zhang, H. Yan, J.R. Gong, J. Am. Chem. Soc. 133 (2011) 10878–10884.
[26] I.V. Lightcap, T.H. Kosel, P.V. Kamat, Nano Lett. 10 (2010) 577–583.
[27] F. Meng, J. Li, S.K. Cushing, M. Zhi, N. Wu, J. Am. Chem. Soc. 135 (2013) 10286–10289.
[28] Q. Xiang, J. Yu, M. Jaroniec, Chem. Soc. Rev. 41 (2012) 782–796.
[29] L. Duan, F. Bozoglian, S. Mandal, B. Stewart, T. Privalov, A. Llobet, L. Sun, Nat. Chem. 4 (2012) 418.
[30] B.H. Meekins, P.V. Kamat, J. Phys. Chem. Lett. 2 (2011) 2304–2310.
[31] A. Li, T. Wang, X. Chang, W. Cai, P. Zhang, J. Zhang, J. Gong, Chem. Sci. 7 (2016) 890–895.
[32] S. Anantharaj, K. Karthick, S. Kundu, Mater. Today Energy 6 (2017) 1–26.
[33] M. Shao, F. Ning, M. Wei, D.G. Evans, X. Duan, Adv. Funct. Mater. 24 (2014) 580–586.
[34] L. Mohapatra, K. Parida, J. Mater. Chem. A 4 (2016) 10744–10766.
[35] D.H. Youn, Y.B. Park, J.Y. Kim, G. Magesh, Y.J. Jang, J.S. Lee, J. Power Sources 294 (2015) 437–443.
[36] F. Dionigi, P. Strasser, Adv. Energy Mater. 6 (2016) 1600621.
[37] H. Qi, J. Wolfe, D. Fichou, Z. Chen, Sci. Rep. 6 (2016) 30882.
[38] L. Wang, F. Dionigi, N.T. Nguyen, R. Kirchgeorg, M. Gliech, S. Grigorescu, P. Strasser, P. Schmuki, Chem. Mater. 27 (2015) 2360–2366.
[39] F. Ning, M. Shao, S. Xu, Y. Fu, R. Zhang, M. Wei, D.G. Evans, X. Duan, Energy Environ. Sci. 9 (2016) 2633–2643.
[40] X. Yu, P. Yang, S. Chen, M. Zhang, G. Shi, Adv. Energy Mater. 7 (2017) 1601805.
[41] Z. Lu, L. Qian, Y. Tian, Y. Li, X. Sun, X. Duan, Chem. Commun. 52 (2016) 908–911.
[42] X. Wang, Y. Liang, W. An, J. Hu, Y. Zhu, W. Cui, Appl. Catal. B: Environ. 219 (2017) 53–62.
[43] H. Wang, Y. Liang, L. Liu, J. Hu, P. Wu, W. Cui, Appl. Catal. B: Environ. 208 (2017) 22–34.
[44] Z. Hua, X. Zhang, X. Bai, L. Lv, Z. Ye, X. Huang, J. Colloid Interface Sci. 450 (2015) 45–53.
[45] N. Han, F. Zhao, Y. Li, J. Mater. Chem. A 3 (2015) 16348–16353.
[46] S. Nayak, L. Mohapatra, K. Parida, J. Mater. Chem. A 3 (2015) 18622–18635.
[47] T. Tanaka, Y. Kameshima, S. Nishimoto, M. Miyake, Anal. Methods 4 (2012) 3925–3927.
[48] F.X. Zhang, J. Lian, U. Becker, R.C. Ewing, L.M. Wang, J. Hu, S.K. Saxena, J. Solid State Chem. 180 (2007) 571–576.
[49] J. Takahashi, T. Ohtsuka, J. Am. Ceram. Soc. 72 (1989) 426–431.
[50] S. Hu, B. Chi, J. Pu, L. Jian, RSC Adv. 4 (2014) 60437–60444.
[51] C. Tang, H.-S. Wang, H.-F. Wang, Q. Zhang, G.-L. Tian, J.-Q. Nie, F. Wei, Adv. Mater. 27 (2015) 4516–4522.
[52] R. Boppella, A. Mohammadpour, S. Illa, S. Farsinezhad, P. Basak, K. Shankar, S.V. Manorama, Acta Mater. 119 (2016) 92–103.
[53] S. Illa, R. Boppella, S.V. Manorama, P. Basak, J. Phys. Chem. C 120 (2016) 18028–18038.
[54] Y.-C. Chen, Y.-C. Pu, Y.-J. Hsu, J. Phys. Chem. C 116 (2012) 2967–2975.
[55] J. Guo, C. Mao, R. Zhang, M. Shao, M. Wei, P. Feng, J. Mater. Chem. A 5 (2017) 11016–11025.
[56] J. Hou, H. Cheng, O. Takeda, H. Zhu, Angew. Chem. Int. Ed. 54 (2015) 8480–8484.
[57] W. Li, P. Da, Y. Zhang, Y. Wang, X. Lin, X. Gong, G. Zheng, ACS Nano 8 (2014) 11770–11777.
[58] G. Ai, R. Mo, H. Li, J. Zhong, Nanoscale 7 (2015) 6722–6728.
[59] M. Zhou, J. Bao, W. Bi, Y. Zeng, R. Zhu, M. Tao, Y. Xie, ChemSusChem 5 (2012) 1420–1425.
[60] M.A. Butler, D.S. Ginley, J. Electrochem. Soc. 125 (1978) 228–232.
[61] R. Boppella, K. Anjaneyulu, P. Basak, S.V. Manorama, J. Phys. Chem. C 117 (2013) 4597–4605.
[62] R. Boppella, P. Basak, S.V. Manorama, ACS Appl. Mater. Interfaces 4 (2012) 1239–1246.
[63] Q. Xiang, J. Yu, M. Jaroniec, J. Phys. Chem. C 115 (2011) 7355–7363.
[64] Q. Xiang, J. Yu, M. Jaroniec, Nanoscale 3 (2011) 3670–3678.
[65] D. Friebel, M.W. Louie, M. Bajdich, K.E. Sanwald, Y. Cai, A.M. Wise, M.-J. Cheng, D. Sokaras, T.-C. Weng, R. Alonso-Mori, R.C. Davis, J.R. Bargar, J.K. Nørskov, A. Nilsson, A.T. Bell, J. Am. Chem. Soc. 137 (2015) 1305–1313.
[66] Z. Qin, Y. Chen, Z. Huang, J. Su, L. Guo, J. Mater. Chem. A 5 (2017) 19025–19035.
[67] M. Yoon, Y. Oh, S. Hong, J.S. Lee, R. Boppella, S.H. Kim, F. Marques Mota, S.O. Kim, D.H. Kim, Appl. Catal. B: Environ. 206 (2017) 263–270.